A Multiscale Numerical Study of Hurricane Andrew (1992). Part II: Kinematics and Inner-Core Structures

Yubao Liu

Department of Atmospheric and Oceanic Sciences, McGill University, Montreal, Quebec, Canada

Da-Lin Zhang

Department of Meteorology, University of Maryland, College Park, Maryland

M. K. Yau

Department of Atmospheric and Oceanic Sciences, McGill University, Montreal, Quebec, Canada

ABSTRACT

Despite considerable research, understanding of the temporal evolution of the inner-core structures of hurricanes is very limited owing to the lack of continuous high-resolution observational data of a storm. In this study, the results of a 72-h explicit simulation of Hurricane Andrew (1992) with a grid size of 6 km are examined to explore the inner-core axisymmetric and asymmetric structures of the storm during its rapid deepening stage. Based on the simulation, a conceptual model of the axisymmetric structures of the storm is proposed. Most of the proposed structures confirm previous observations. The main ingredients include a main inflow (outflow) in the boundary layer (upper troposphere) with little radial flow in between, a divergent slantwise ascent in the eyewall, a penetrative dry downdraft at the inner edge of the eyewall, and a general weak subsiding motion in the eye with typical warming/drying above an inversion located near an altitude of about 2–3 km. The storm deepens as the axes of these features contract.

It is found that the inversion divides the eye of the hurricane vertically into two parts, with a deep layer of warm/dry air above and a shallow pool of warm/moist air below. The air aloft descends at an average rate of 5 cm s^{-1} and has a residency time of several days. In contrast, the warm/moist pool consists of air from the main inflow and penetrative downdrafts, offset somewhat by the air streaming in a returning outflow into the eyewall in the lowest 2 km; it is subject to the influence of the upward heat and moisture fluxes over the underlying warm ocean. The warm/moist pool appears to play an important role in supplying high-θ_e air for deep convective development in the eyewall. The penetrative downdraft is dry and originates from the return inflow in the upper troposphere, and it is driven by sublimative/evaporative cooling under the influence of the (asymmetric) radial inflow of dry/cold air in the midtroposphere. It penetrates to the bottom of the eye (azimuthally downshear with a width often greater than 100 km) in a radially narrow zone along the slantwise inner edge of the eyewall.

It is further shown that all the meteorological fields are highly asymmetric. Whereas the storm-scale flow features a source–sink couplet in the boundary layer and dual gyres aloft, the inner-core structures exhibit alternative radial inflow and outflow and a series of inhomogeneous updrafts and downdrafts. All the fields tilt more or less with height radially outward and azimuthally downshear. Furthermore, pronounced fluctuations of air motion are found in both the eye and the eyewall. Sometimes, a deep layer of upward motion appears at the center of the eye. All these features contribute to the trochoidal oscillation of the storm track and movement. The main steering appears to be located at the midtroposphere (~4.5 km) and the deep-layer mean winds represent well the movement of the hurricane.

1. Introduction

Hurricanes typically occur on a scale of several hundred kilometers. However, the most severe convective activity and devastating winds are concentrated in the inner-core region. This region encompasses the eye, eyewall, and spiral rainbands and lies within a radius of 100 km from the center of the storm. In some cases, when the hurricane deepens rapidly and achieves great intensity, its eye can shrink to a radius of 10 km. It is within the inner-core region that the major energy generation and conversion processes take place to drive the entire hurricane system (see the review by Anthes 1982;

Corresponding author address: Dr. Da-Lin Zhang, Department of Meteorology, University of Maryland, 3433 Computer and Space Sciences Building, College Park, MD 20742-2425.
E-mail: dalin@atmos.umd.edu

Willoughby 1995). The violent and complicated dynamical and physical processes associated with the inner-core circulations have captivated the attention of researchers in the past decades.

Earlier studies on the inner core of hurricanes began shortly after World War II when instrumented aircraft, equipped with airborne radar and in situ instruments, penetrated into the storms. Riehl (1954) summarized some earlier findings on the basic structures of the eye, the eyewall, and the circular high-wind zones. Shea and Gray (1973) carried out a composite analysis on aircraft data obtained from over 500 radial flight legs in 22 Atlantic storms during the period 1957–69. They reported many significant features of the inner-core circulations, including the shallow but intense near-surface inflow, the radius of maximum wind (RMW), the large D-values, the intense temperature gradients, and the strong convergence and upward motion in the eyewall. Gray and Shea (1973) showed that the maximum temperatures in the inner core do not occur in regions of intense updrafts but reside inside the eye, and arise from the sinking motion in the eye rather than from thermal diffusion from the eyewall updrafts. Using improved in situ observations in Hurricanes Anita (1977), David (1979), Frederic (1979), and Allen (1980), Willoughby et al. (1982) documented the existence of concentric eyewall structures and confirmed the eyewall contraction theory of Shapiro and Willoughby (1982) that was proposed to explain the rapid development of the primary circulation in hurricanes (Willoughby 1990; Willoughby and Black 1996). Jorgensen (1984a,b) analyzed in great detail the structures and evolution of clouds and precipitation in the inner cores of the above mentioned storms. He found intense deep convection located in the eyewall and weaker stratiform rainfall outside. He also noted the presence of strong cyclonic shear and substantial radial convergence along the inner edge of the eyewall.

While aircraft observations are limited to sampling only a small portion of a hurricane, airborne Doppler radar can provide a three-dimensional (3D) description of its flow structure over a large area. For example, Marks and Houze (1987) constructed the primary and secondary circulations of Hurricane Alicia (1983) using airborne Doppler radar measurements. They found that the secondary circulation is characterized by inward flows crossing the eyewall in the marine boundary layer (MBL) and concentrated intense outflows above 12 km. The motion in a vertical cross section resembles that of a squall line with dominant downdrafts below the melting level and mesoscale downdrafts at the base of the stratiform region. Based on high-resolution radar data obtained through repeated inner-core penetrations, Marks et al. (1992) studied the axisymmetric and asymmetric nature of Hurricane Norbert (1984) and documented significant 3D variations in the tangential and radial winds. These asymmetric flow structures have a strong influence on the distribution of ice particles and precipitation (Houze et al. 1992) and affect significantly the calculation of the water budget (Gamache et al. 1993).

In precipitation-free regions (e.g., the eye) and in the lowest 0.5 km of the MBL where sea clutter occurs, the usefulness of Doppler radar is severely curtailed. Thus, dropwindsonde observations have been used to examine the dynamics and thermodynamics of the eye (Riehl 1948; Simpson 1952; Stear 1965), and surface-based instruments have been developed to investigate the air–sea interaction in the MBL. Early studies showed that the eye is characterized by relatively weak circulation with the warm and moist air underlying the warm but dry air in the midtroposphere. Based on two dropwindsonde observations in the eye of Hurricane Gloria (1985), Franklin et al. (1988) noted dramatic thermodynamic changes as a result of fluctuating vertical motions, which range from a descent of 30 hPa h^{-1} at one instant to an ascent of 10 hPa h^{-1} at 500 hPa at another time. Nevertheless, no instruments have provided a complete three-dimensional description of the airflow in the inner-core and outer regions of a hurricane.

Parallel to the observational studies are various theoretical investigations devoted to various aspects of the inner-core dynamics. Examples include studies on the secondary circulation (Willoughby 1979; Schubert and Hack 1982), concentric eyewall and eyewall contraction (Shapiro and Willoughby 1982), air–sea interaction (Emanuel 1986), balanced flows (Shapiro and Montgomery 1993), spiral rainbands (Willoughby 1979; Guinn and Schubert 1993), and the dynamics of the eye (Willoughby 1979; Smith 1980; Emanuel 1997). Similarly, high-resolution numerical models have been developed to examine the mechanism(s) by which various inner-core elements are generated under idealized conditions (Kurihara and Bender 1982; Willoughby et al. 1984a; Rotunno and Emanuel 1987; Tripoli 1992; Nicholls and Pielke 1995) and observed initial conditions (Eastman 1995; Liu et al. 1997).

Despite considerable progress, much remains unknown about the inner-core structures of hurricanes. Some unanswered questions include the following: what is the spatial distribution and temporal variation of vertical motion in the eye, above and beyond the overall ''subsidence''? Is there any mass exchange between the eye, eyewall, and the outer regions? How do the axisymmetric and the asymmetric flows vary with time and space? The purpose of this paper is to shed light on the above questions from an analysis of a 72-h (1200 UTC 21 August–1200 UTC 24 August 1992), triply nested-grid simulation of Hurricane Andrew (1992). The run was carried out using the state-of-the-art Pennsylvania State University–National Center for Atmospheric Research nonhydrostatic model (i.e., MM5) with the finest grid mesh at 6 km. We demonstrated in Part I (Liu et al. 1997) that the model reproduces reasonably well the track and intensity, as well as the structures of the eye, eyewall, spiral rainbands, RMW, and other inner-core

features as compared to available observations and the results of previous hurricane studies. Thus, our simulation provides a complete four-dimensional, dynamically consistent dataset useful in gaining insight into the inner-core structures and evolution of a hurricane.

The next section presents the methodology used to process the model data. Section 3 shows the zonal mean flow in relation to the movement of the storm and the hurricane's axisymmetric mean structures as compared to previous studies. Section 4, which is the main focus of this paper, deals with the contraction of the eyewall, the gravitational oscillations in the eye, and the thermodynamic properties and the vertical motion in the eye. A conceptual model for the eye and eyewall will also be presented. Section 5 is devoted to an examination of the asymmetric characteristics and their impact on the movement of the storm. A summary and concluding remarks are given in the final section.

2. Analysis procedures

In this study, we will use the hourly model output in (x, y, σ) coordinates from the 6-km resolution domain. There are $124 \times 94 \times 23$ points covering a horizontal area of 738 km $\times$ 548 km. This domain was activated for 45 h, starting from 27 h (unless specified otherwise, hereafter the hours will refer to the hours into the integration) when a substantial amount of gridscale condensation occurred in the eyewall over the intermediate (18 km) resolution domain (see Liu et al. 1997 for more details). In the 6-km domain, the predicted variables are the horizontal winds (U, V), vertical velocity (W), temperature (T), atmospheric pressure (p), the mixing ratios of water vapor (q_v), cloud water (q_c), cloud ice (q_i), rainwater (q_r), snow (q_s), and graupel (q_g). Because of the dominant axisymmetric nature of hurricanes, it is convenient to discuss the inner-core structures in cylindrical coordinates. For this purpose, all prognostic variables within a radius of 180 km from the center of the surface low are transformed from the model (x, y, σ) coordinates to cylindrical (r, θ, z) coordinates. To preserve the high-resolution simulation in the MBL, all derived variables are calculated first on the model grids and then interpolated onto the cylindrical coordinates.

To better understand the inner-core structures of the storm, we follow the procedures of Marks et al. (1992) and Roux and Viltard (1995) to decompose the transformed model variables into their axisymmetric and asymmetric components. For a scalar, X, we write

$$X = X_s + X_a, \tag{1}$$

where the axisymmetric (X_s) component is given by

$$X_s(r, z) = \frac{1}{2\pi} \int_0^{2\pi} X(r, \theta, z) \, d\theta, \tag{2}$$

and the asymmetric (X_a) component can be computed as

$$X_a(r, \theta, z) = X - X_s. \tag{3}$$

For the horizontal wind velocity $\mathbf{V}$, we first define a deep-layer mean velocity $\mathbf{V}_m$ by

$$\mathbf{V}_m = \frac{\int_{900\,\text{hPa}}^{150\,\text{hPa}} \int_0^{2\pi} \int_0^{150\,\text{km}} \mathbf{V} r \, dr \, d\theta \, dp}{\int_{900\,\text{hPa}}^{150\,\text{hPa}} \int_0^{2\pi} \int_0^{150\,\text{km}} r \, dr \, d\theta \, dp}. \tag{4}$$

We then calculate

$$\mathbf{V}' = \mathbf{V} - \mathbf{V}_m, \tag{5}$$

from which we obtain the tangential and the radial winds V_t' and V_r'. Finally we write

$$V_t' = (V_t')_s + (V_t')_a \tag{6a}$$

$$V_r' = (V_r')_s + (V_r')_a \tag{6b}$$

with the axisymmetric components $[(V_t')_s, (V_r')_s]$ and the asymmetric components $[(V_t')_a, (V_r')_a]$ calculated, respectively, in a manner similar to Eqs. (2) and (3).

Note that $\mathbf{V}_m$ denotes a deep-layer domain-averaged velocity in the layer between 900 and 150 hPa over an area within a radius of 150 km around the core. We have varied the radius in the integration from 100 to 180 km and found little variation in the results.

3. Area-averaged mean flow and axisymmetric structures

a. Area-averaged mean flow and hurricane movement

Previous studies have revealed that the environmental flow and the vertical shear affect significantly the movement and asymmetric structures of hurricanes (Marks et al. 1992; Franklin 1990; Franklin et al. 1993; Bender 1997). Traditionally, the steering of a storm is estimated by averaging the geostrophic winds in an annulus at a radius of several degrees of latitude from its center (see Elsberry 1995). Recently, using high-resolution Doppler observations in hurricane cores, Marks et al. (1992) found that the deep-layer mean wind averaged within a radius of 39 km from the storm center depicts quite accurately the steering of Hurricane Norbert (1984). Since MM5 simulates reasonably well the track and propagation of Andrew, it is of interest to examine how its movement is affected by the environmental flows.

Figure 1 displays the time–height cross sections of the area-averaged ground- and storm-relative mean winds. The mean environmental flows exhibit significant directional and speed shears (Fig. 1a). An easterly flow (mostly around 6 m s^{-1}) prevails in a deep layer below 9 km, with a shallow layer of strong winds at 2 km. Higher up, the wind veers to southeasterly at 12 km, before it backs to an easterly direction at 14 km and finally to a northeasterly flow near the model top. The vertical profile of the mean wind is similar to that
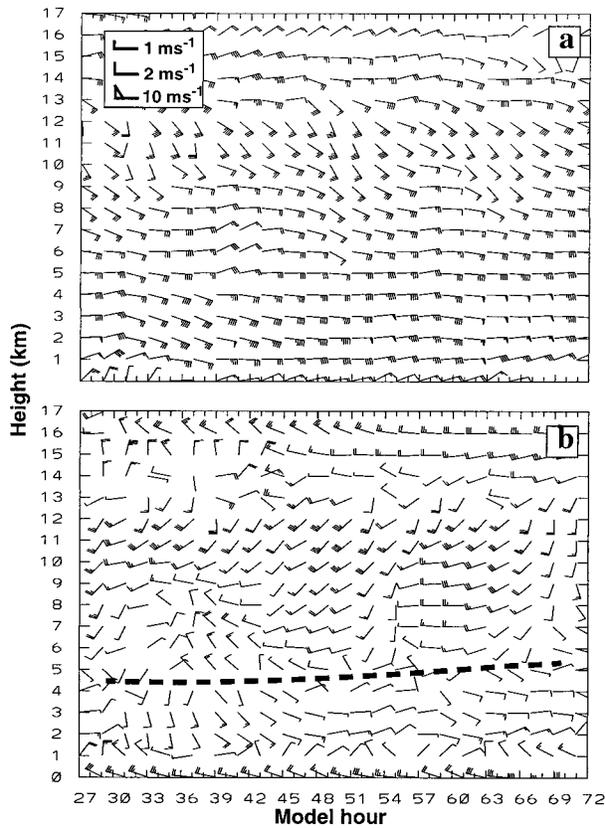
FIG. 1. The time–height cross section of the (a) total and (b) storm-relative winds averaged within a radius of 150 km from the center of the simulated Andrew. A pennant, a full barb, and a half barb represents 10, 2, and 1 m s⁻¹, respectively. Thick-dashed lines in (b) denote the steering level of the storm.

observed in other hurricanes (e.g., see Marks et al. 1992; Roux and Viltard 1995).

Except in the MBL, the storm-relative mean winds (Fig. 1b) are generally quite weak in the lowest 9 km, with most values being less than 2 m s⁻¹. A significant implication is that the mean flow below 9 km may be responsible for the steering of the storm. A careful examination reveals that there are three distinct layers in the steering flow: a northwesterly layer in the MBL, a southwest to westerly layer above 4.5 km, and a southeast to easterly layer in between. The movement of the storm is therefore close to the area-averaged wind in the layer from 4 to 5 km. There is a net westerly inflow due to frictional convergence in the MBL, a net easterly inflow between 1 and 4.5 km, and a net southwesterly inflow aloft.

Figure 2a compares the time evolution of the translation velocity ($\mathbf{V}_s$) of the simulated storm to that of the mass-weighted deep-layer mean velocity [$\mathbf{V}_m$, Eq. (4)]; the difference wind vectors are also plotted. We have removed the trochoidal oscillation to obtain the storm translation speed (see section 6 for more details). Except before 31 h, the deep-layer mean winds are very close

to the storm translation velocity, the difference in speed is generally less than 1.5 m s⁻¹ (Fig. 2b). The averaged winds even capture well the amplitude and phase of the temporal fluctuation in translation during the 45-h period. These results are in agreement with the findings of Marks et al. (1992), and they are also consistent with previous studies on the steering flow of hurricanes (e.g., George and Gray 1976; Holland 1984; Dong and Neumann 1986). The results suggest that a dense array of dropwindsonde observations in the inner-core region might be used to provide a reasonable short-term prediction of hurricane tracks, assuming a steady translation of the storm.

b. Mean axisymmetric structures

Figure 3 shows the simulated mean axisymmetric flow structures of Hurricane Andrew (1992). During this 12-h period, the central pressure of the model hurricane reaches a value less than 950 hPa and a maximum surface wind greater than 65 m s⁻¹. Clearly, such spatial and temporal averages tend to suppress some transient and smaller-scale (asymmetric) signals, but the persistent and organized features should be well retained.

In general, the axisymmetric mean thermodynamic and precipitation structures are similar to their instantaneous fields (see Part I). For example, the axisymmetric radar reflectivity (Fig. 3a), which is derived from the model precipitation fields (see Part I), has features of a clear eye, an outward sloping eyewall with sharp gradients at the inner edge, a high concentration of precipitation below the 0°C isotherm (near 4.5 km) with maximum intensity (>45 dBZ) in the lowest 1 km, and a decrease in the amount of precipitation with increasing radius. Similar structures also appear in the mean relative humidity field (Fig. 3b). The driest air (RH < 5%) is located in the eye and the highest humidity (>95%) appears in the eyewall. Of interest is the "bright band" associated with the melting of ice particles that is still evident below the 0°C isotherm in spite of the extensive averaging. This melting effect causes notable cooling (Fig. 3d) and an accompanying increase in relative humidity because of the decrease in saturation vapor pressure (Fig. 3b). A region of slightly enhanced inward radial inflow (Fig. 3f) near the 0°C level at 60–120-km radius can also be noted.

The equivalent potential temperature, θ_e, increases toward the center in the boundary layer as a result of upward latent and sensible heat fluxes[1] when air parcels

---

[1] The relative contribution of upward sensible and latent heat fluxes to the net increase in θ_e, as a parcel moves from the outer region (say, at $R = 150$ km) to the center of the eye, can be estimated with the following equation:

$$\Delta \theta_e = \frac{L}{C_p} \frac{\overline{\theta_e}}{\overline{T}} \Delta q_v + \frac{\overline{\theta_e}}{\overline{T}} \Delta T - \frac{R}{C_p} \frac{\overline{\theta_e}}{\overline{p}} \Delta p,$$
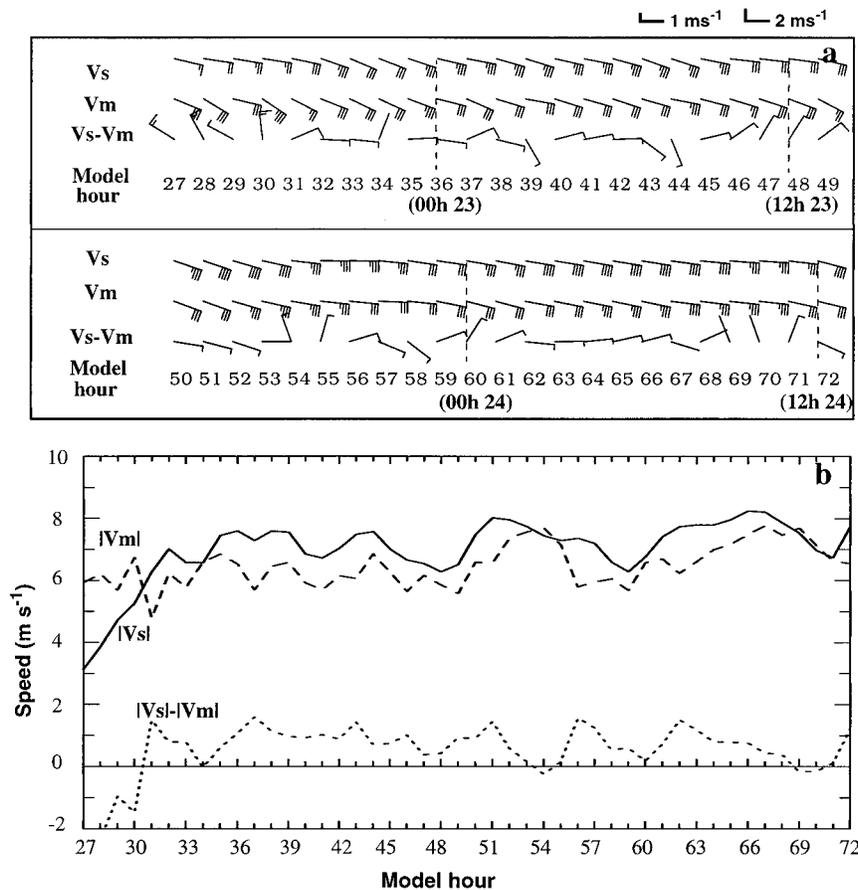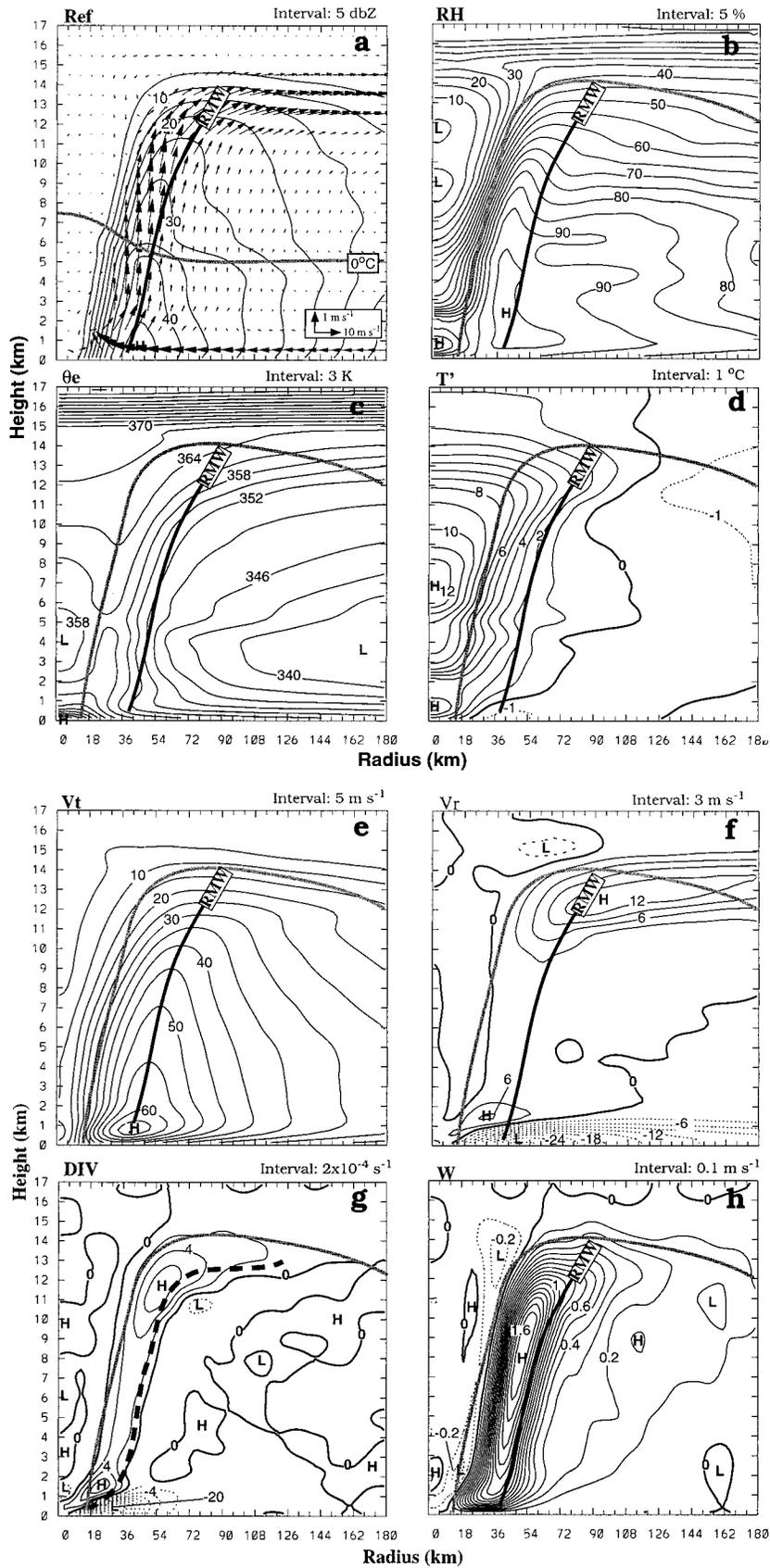
FIG. 2. A comparison of (a) the hourly mean velocity ($\mathbf{V}_m$, averaged from the profile given in Fig. 1 between 900 and 150 hPa) and the propagation velocity ($\mathbf{V}_s$) and (b) their speeds (i.e., $|\mathbf{V}_s|$, $|\mathbf{V}_m|$) and differences (i.e., $|\mathbf{V}_s| - |\mathbf{V}_m|$) of the simulated Andrew. A full barb and a half barb in (a) represents 2 and 1 m s^{-1}, respectively.

accelerate toward the eyewall (cf. Figs. 3c and 3f). A particularly pronounced increase in θ_e occurs as the parcels decelerate after passing the RMW. A maximum value ($\theta_e = 385$ K) is located at the storm center, corresponding to a warm and moist anomaly (cf. Figs. 3b–d). This air–sea interaction process helps maintain the large potential instability in the outer environment

and feed energy to the eyewall convection through slantwise ascent in an area of divergent outflow (Figs. 3f–h). A layer of midtropospheric minimum θ_e persists in the eye at all times, which is typical of many hurricanes (e.g., Hawkins and Imbembo 1976). The downward dip of high θ_e at the upper level and an upward tilt of the high-θ_e axis near a radius of 24 km along the inner edge of the eyewall are associated, respectively, with the subsidence of air mass from the upper troposphere and the upward transport of high-θ_e air from the bottom of the eye into the eyewall (cf. Figs. 3c and 3h).

The mean temperature anomaly, defined at each level as the deviation from the temperature averaged over a horizontal area within a radius of 180 km, shows an intense warm core with a maximum warming of 12°C at 7 km (about 425 hPa; see Fig. 3d), which is 6 km lower than that used by Emanuel (1986) and Holland (1997) in their estimating the maximum intensity of tropical cyclones. (This implies that intense vertical shear in tangential winds in their studies tends to occur in the upper troposphere, based on the thermal wind approximation.) The average horizontal thermal gradi-

where the overbar quantities represent mean values over the transit and all the symbols assume their usual meteorological meaning. We have also assumed that $\overline{T_c} = \overline{T}$, where $\overline{T_c}$ denotes the averaged isentropic condensation temperature. Equation (7) states that the θ_e increase, following a surface air parcel, can occur as a result of moistening through latent heat flux, warming through sensible heat flux, and isothermal expansion. From the associated model output of Fig. 3c, we have the surface values of $\theta_e = 351.8$ K, $P = 1001.6$ hPa, $T = 299.2$ K, and $q_v = 18.9$ g kg^{-1} at $R = 150$ km and their surface values at $R = 0$ km of 385 K, 931.7 hPa, 303.0 K, and 25.7 g kg^{-1}, respectively. With these values, the above equation gives an increase in θ_e of 33.5 K at the eye center caused by the isothermal expansion (7.3 K), sensible heat (4.6 K), and latent heat (21.6 K) fluxes. This 33.5-K increase in θ_e is very close to the θ_e difference of 33.2 K between $R = 0$ and $R = 150$ km in the model.

ent amounts to about 12°C/75 km, a value much larger than that in most observed atmospheric fronts. An inversion is located in the eye from 2 to 4 km in altitude and its strength decreases outward. The inversion imposes resistance to W in the eye and it tends to separate the extremely dry air aloft from the moist air below (cf. Figs. 3c,d). Furthermore, the inversion acts as a "lid" to suppress deep convective overturning and allows only the development of the frequently observed boundary layer stratiform clouds in the eye (Jordan 1952).

The mean axisymmetric tangential flow represents the primary circulation of a hurricane. It is characterized by a ring of intense flow with a maximum (>65 m s^{-1}) at 39-km radius and about 800 m above the surface (Fig. 3e). Its maximum slopes outward with height up to 10 km and lies in close proximity to the maximum of the simulated radar reflectivity (cf. Figs. 3a,e), which suggests the important role of the RMW in carrying heavy precipitation content. Extremely large vertical shears are present in the MBL, particularly in the eyewall, as a result of surface friction. The (r, z) distribution of the tangential wind bears strong resemblance to that simulated by Kurihara and Bender (1982, see their Fig. 3) with a grid size of 5 km. However, their results give little indication of the sloping structures, such as the slantwise updrafts in the eyewall, probably due to their use of a convective adjustment scheme. This difference points to the necessity of using a fully explicit microphysics approach to simulate realistically the slantwise nature of the eye and the eyewall. Because the maximum tangential wind lies below 1 km, caution must be exercised in converting the flight-level (normally at 700 hPa) winds to surface winds, such as were done in Powell (1982) and Powell and Houston (1996); see Zhang et al. (1999) for a detailed discussion.

The mean radial winds exhibit a layer of intense (convergent) inflow below 1.5 km up to 12-km radius, with the peak value in the surface layer. This result is as expected because it represents the frictionally induced cross-isobaric component of the wind. The maximum inflow (>27 m s^{-1}) is located slightly outward from the central eyewall. A layer of pronounced (divergent) outflow can be found outside a radius of 45 km at altitudes between 11 and 15 km. The layers in between are marked by regions of relatively weak radial outflow (Figs. 3a,f).

It is interesting to note that despite the presence of intense updrafts, the radial winds in the eyewall are divergent, *even in the layers where the updraft accelerates with height,* except in the (4–5 km) melting layer (cf. Figs. 3f,g). The deep-layer divergence is a consequence of the slantwise nature of deep convection in the eyewall where the air converges into the core of updrafts in low levels and diverges in a shallower layer aloft (Fig. 3g). In the eye, there are two airstreams worthy of discussion. The first is the divergent outflow of moderate intensity that slopes into the eyewall from the bottom of the eye center, which will be referred to as the low-level return outflow (RO). As will be shown in a forthcoming article, this RO is highly supergradient and it results from the transfer of angular momentum by the secondary circulation in the MBL. This stream appears to play an important role in (a) drawing air out of the eye to reduce the central pressure, and (b) transporting high-θ_e air from the bottom of the eye to support partly eyewall convection (cf. Figs. 3c and 3f,g). The second airstream is the upper-level returning inflow (RI) within a radius of 96 km into the eye; it lies above the region of the main upper outflow with a magnitude of about 3 m s^{-1} at an altitude of 15 km. The RI constitutes part of the divergent outflow above the intense updrafts in the eyewall (see Fig. 10a). It represents a source of mass for the eye (in an azimuthally averaged sense) and partially feeds the penetrative downdraft at the inner edge of the eyewall (cf. Figs. 3f–h).

Figure 3h shows intense slantwise upward motion in the eyewall with the averaged peak intensity >1.6 m s^{-1} at 8 km and much weaker upward motion in the outer spiral-band regions. The deep, intense updraft in the eyewall is rooted in the boundary layer, with mass and energy fed in by the inward convergence of the MBL air and by the RO immediately above in the eye. In contrast, the upper-level outflow represents a sink of mass for the storm. In this sense, the eyewall updraft is a manifestation of slantwise convection that plays a role in ventilating the mass throughout the troposphere and in rendering the atmospheric stratification slantwise neutral with respect to absolute momentum surfaces in the eyewall. At the top of the eyewall, some mass is returned to the eye. The returned mass sinks in a narrow zone (but with an azimuthal width greater than 100 km; see Fig. 10f) at the inner edge of the eyewall and reaches down to the MBL where it reenters the eyewall (cf. Figs. 3f–h). This pronounced subsidence near the eyewall has been noted in recent observations (e.g., Jorgensen 1984b; Marks et al. 1992). Its existence is also supported by the appearance of the downward dip in the θ_e field at the inner edge of the eyewall (cf. Figs. 3c,h) and trajectory calculations (not shown). The confinement of the intense subsidence to a narrow zone in the vertical

←

FIG. 3. Radius–height cross sections of azimuthally and temporally (from the 48- to 60-h integration) averaged fields: (a) radar reflectivity (Ref, dBZ), (b) relative humidity (RH, %), (c) equivalent potential temperature (θ_e, K), (d) temperature deviation (T', °C), (e) tangential winds (V_t, m s^{-1}), (f) radial winds (V_r, m s^{-1}), (g) divergence (DIV, 10^{-4} s^{-1}), and (h) vertical velocity (W, m s^{-1}). Thick solid lines denote the distribution of 0°C, the inner edge of the eyewall by the 10-dbZ contour, and the RMW. Thick dashed lines in (g) is the axis of maximum updrafts from (h). Solid (dashed) lines represent positive (negative) values.
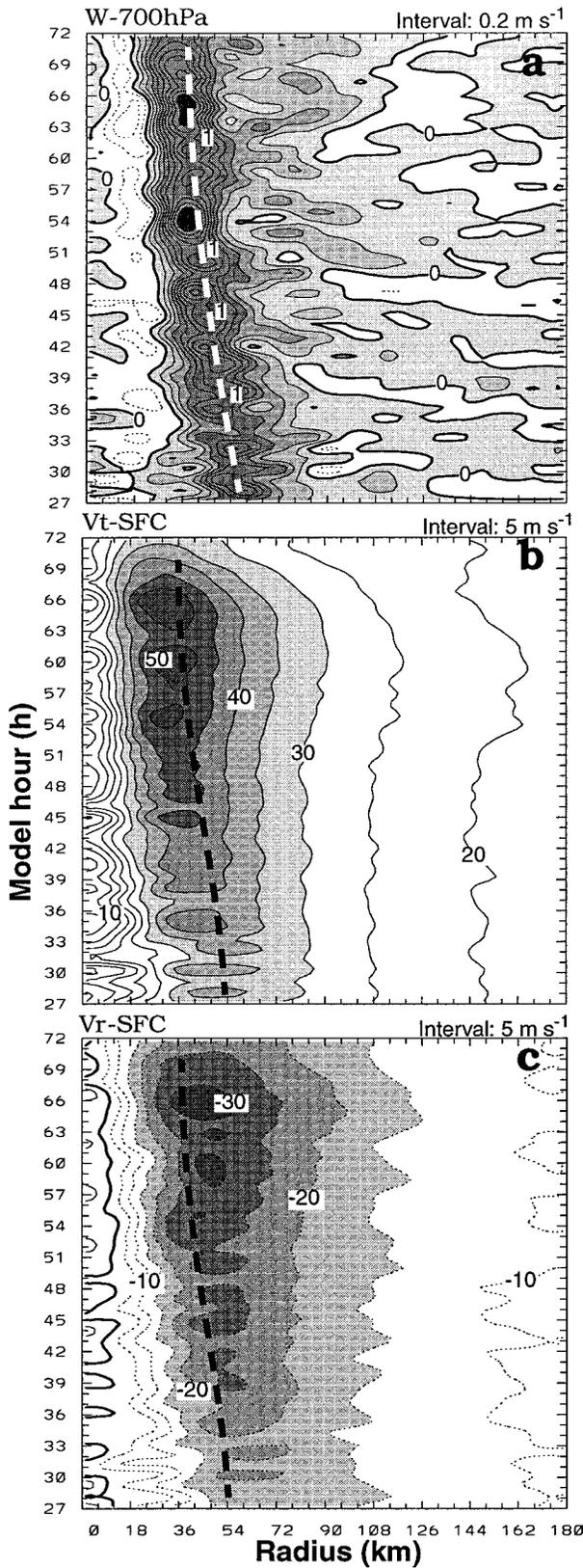
FIG. 4. The time–radius cross section of azimuthally averaged fields: (a) vertical motion at 700 hPa, and (b) tangential and (c) radial

is due partly to the presence of large inertial stability within the RMW and partly to the sublimative/evaporative cooling at the cloud edge. Cooling below the melting layer (see Fig. 3d) appears to enhance the subsidence at the inner edge and accounts for the secondary downdraft maximum around 2 km.

4. Structure and evolution of the inner core

a. Contraction of and fluctuations in the eyewall

Willoughby et al. (1982) and Willoughby and Black (1996) documented the contraction of the eyewall in several hurricanes, including the present storm. To gain insight into the basic processes involved in the contraction, Figure 4 shows the time–radius cross section of the axisymmetric components of W at 700 hPa, the surface tangential winds, and the surface radial winds between 27 and 72 h. Because the finest mesh C grid is activated at 27 h, all fields experience some adjustment as the grid resolution increases from 18 to 6 km (see Part I). Nevertheless, one can see clearly the decrease of the radius of the eyewall updraft from 60 to 35 km during the 45-h period. The downdraft at the inner edge of the eyewall, as shown in Fig. 3h, also shrinks in radius. It is important to note that as the eyewall contracts, its updraft and the associated downdraft in the eye intensify until landfall at 68 h. The azimuthally averaged updraft peaks at 2 m s^{-1} at 54 h when Andrew becomes a near-category-5 hurricane (see Part I) and another peak of 2 m s^{-1} occurs just before landfall. Of further importance is that while this updraft and downdraft couplet intensifies with time, the widths, which are about 25 and 12 km, respectively, change little during the 45-h period. It is important to note that a model with a grid size of 6 km can just resolve reasonably the width of the eyewall. The observed width in Andrew is smaller and it could be resolved better with a higher-resolution grid.

Similarly, the radius of maximum tangential wind (or the RMW) at the surface shrinks, for example, from 50 km at 27 h to 30 km at 70 h (i.e., 2 h after landfall; see Fig. 4b), while the maximum surface wind increases persistently to >58 m s^{-1} prior to landfall at 68 h. Thereafter, the sudden increase in surface friction and decrease in surface heat fluxes rapidly weaken the tangential winds of the storm. In contrast, the flows in the outer region (>40 km) remain nearly constant out to 50 h and then intensify steadily until landfall, albeit at a small rate. This increase of surface winds at the outer region indicates that the storm has reached its mature stage, as defined by Holland and Merrill (1984).

In response to the decreasing RMW and increasing

←

wind speeds at the surface ($\sigma = 0.995$). The thick-dashed lines denote the RMW at 700 hPa (a) and the surface (b), (c).
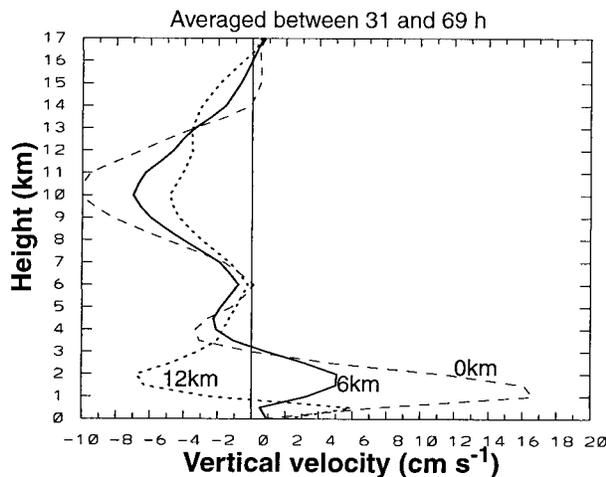
FIG. 5. Vertical profiles of vertical velocity averaged between the 31- and 69-h integrations within a radius of 0 (dashed), 6 (solid), and 12 (dotted) km from the center of the simulated Andrew.

tangential winds, the surface radial inflow also contracts toward the center, and its amplitude doubles from 15 to 30 m s^{-1} in 45 h (Fig. 4c). Note that the axis of the radial inflow is about 12 km outward from the RMW and it is located outside the eyewall. Inside the eyewall, the radial flow decelerates rapidly inward at a rate much greater than its inward acceleration outside the eyewall. The rapid deceleration after passing the RMW explains the large acceleration of updrafts in the lowest 2 km (cf. Figs. 3h and 4c). Note also that the surface inflow penetrates close to the center of the eye throughout the simulation but decreases rapidly upward (cf. Figs. 4c and 3f), which confirms the importance of the friction-induced cross-isobaric component.

It is of interest that as the eyewall shrinks in size and the storm deepens, the time evolution of all the state variables, including the storm's central pressure (see Fig. 2 in Part I), appear to fluctuate in amplitude both in the eye and in the eyewall even in their azimuthal averages (Figs. 4a–c). For example, 14 maxima in the mean updrafts are detectable during the 45-h integration (Fig. 4a) and, thus, have a period of approximately 3 h. These fluctuations result partly from the elliptic shape of the eyewall and the asymmetric distribution of deep convection therein (see Part I), and partly from the propagation of inertial–gravity waves in the eye to be discussed in section 4c.

b. Vertical structure and evolution of the eye

The eye represents one of the most important components in understanding the dynamics and thermodynamics of hurricanes. However, few studies have examined the structures and evolution of the eyes because there were limited observations. Before discussing the simulated vertical structures and evolution, we first examine the mean W at the center of the eye (Fig. 5). The

vertical profiles of vertical velocity averaged over different radii show consistently the presence of subsidence in a deep layer above the inversion at 3-km height, whereas ascent prevails below this level. Peaks can be found at altitudes of 10 and 1.5 km. Clearly, the vertical motion tends to strengthen the inversion as stronger subsidence (>10 cm s^{-1}), similar in magnitude to that computed by Franklin et al. (1988), develops above the warm core located around 7 km (see Fig. 3d). A secondary maximum in subsidence can be found near 4 km where the local static stability is relatively weak (see Fig. 3d). It should be pointed out that in the profile averaged over a radius of 12 km, the descent below 3 km is not representative of the eye because it includes the intense subsidence at the inner edge of the sloping eyewall (see Fig. 3h). The systematic ascent in the lowest layers of the eye depicted at 0- and 6-km radii is generated by the descent near the inner edge of the eyewall, as a result of the mass continuity. The associated air mass diverges cyclonically outward between 1.5 and 4 km (see Fig. 16c in Part I) and forms a local vertical circulation with part of the subsiding air (cf. Figs. 3f–h and 5).

Figure 6 displays the time–height cross section of some thermodynamic properties over an 18 km × 18 km region at the eye center. The temperature anomaly indicates a maximum in the upper troposphere (<15 km altitude) until landfall (Fig. 6a). The magnitude of warm anomaly increases from 5° to 16°C as the storm deepens while the level of maximum anomaly lowers from 11 to 6.5 km during the period from 30 to 66 h. This descent is caused by downward advection of the secluded air in the eye and is, as will be shown later, counteracted somewhat by numerical diffusion. The inversion (displayed in Fig. 3d) is evident between 2 and 3 km and it separates two distinct air masses in the eye. The air below the inversion in the lowest 2 km has upward heat and moisture fluxes from the ocean. Although not as warm as the air above, it is always very moist (Figs. 6a,b). Modulation by fluctuating W can be seen from the moist/cold and dry/warm anomaly couplets in the MBL. The air above the inversion originates from levels higher up, and it dries progressively with time as a result of subsidence. The dry air in the eye extends downward toward the inversion as the storm intensifies.

To further examine the behavior of the air near the center of the eye, we display the evolution of equivalent potential temperature (θ_e) in Fig. 6c. Clearly, θ_e increases with time at each level in the troposphere. However, the exact processes contributing to the increase vary with height. Note first that since the flow in the eye possesses strong cyclonic shear and is inertially stable, the increase in θ_e tends to be dominated more by vertical advection rather than horizontal advective processes (Willoughby 1995). This is generally true except in the minimum θ_e layer, where its horizontal gradient is large, and in the MBL. For example, for the air above the minimum θ_e layer, the downward θ_e displacement,
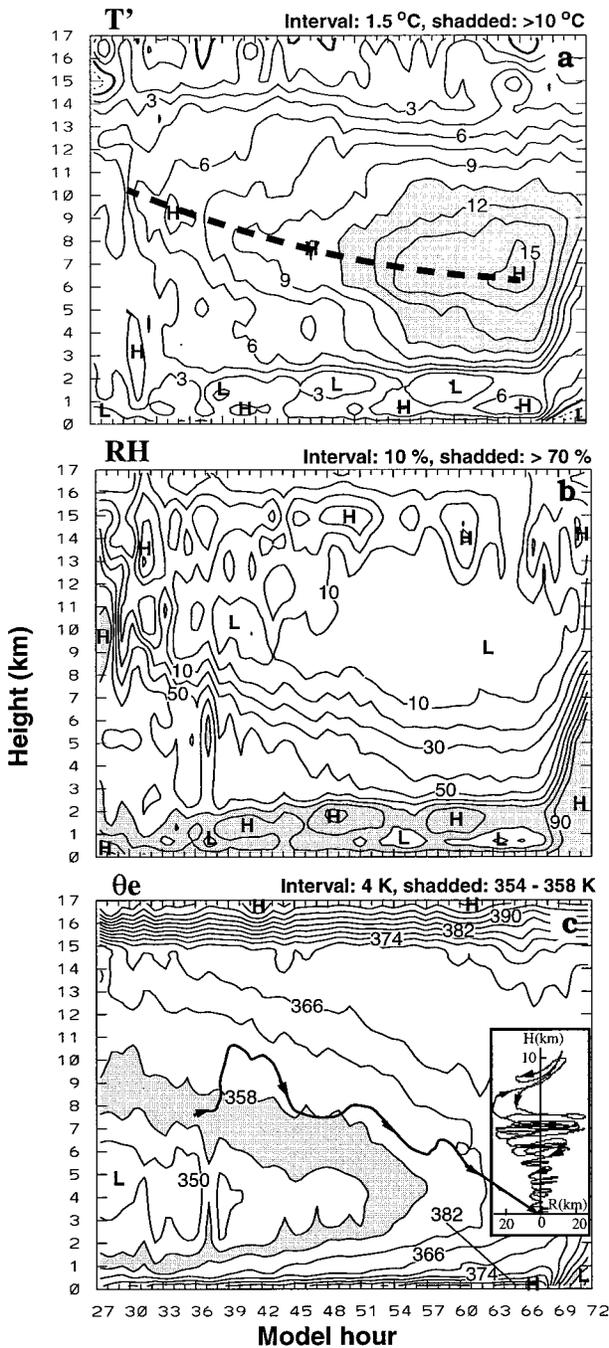
FIG. 6. The time–height cross section for (a) temperature deviation (T', 0°C), (b) relative humidity (RH, %), and (c) equivalent potential temperature (θ_e, K) averaged with nine points (18 × 18 km²) centered in the eye. Superposed on (c) is a backward trajectory (thick solid lines) of an air parcel in the eye, which starts at 3.2 km/68 h backing to 7.5 km/36 h. An inset of the trajectory is also given in (c).
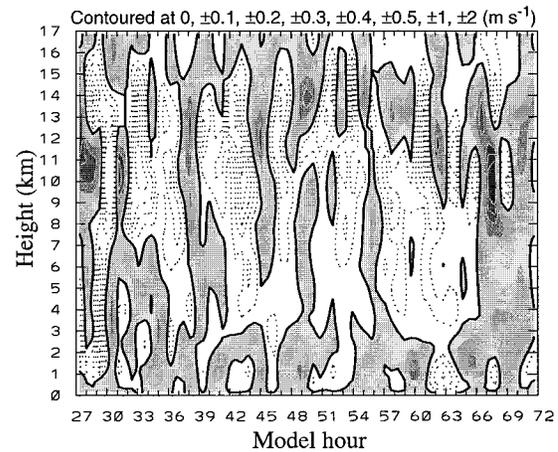

FIG. 7. As in Fig. 6 but for vertical velocity (W, m s⁻¹). Upward motion is shaded.

moisten the core region but damps the magnitude of the warm core. In the inversion layer, the vertical movement of air parcels is limited, so the temperature perturbation and relative humidity remain nearly constant at 2 km (see Figs. 6a,b). Thus, the θ_e increase in the inversion occurs mainly as a result of decreasing pressure as more mass is drawn from the bottom of the eye into the eyewall. In this layer, some portion of the air mass is forced to diverge (see Fig. 3g) slowly or intermittently outward into the descending flow at the inner edge of the eyewall. It follows that the air above the inversion has a very long residence time during the life cycle of the storm. In contrast, the θ_e increases in the MBL (e.g., 24 K from 27 to 68 h) are caused mostly by the surface heat and moisture fluxes and upward advection; so the air mass has much shorter history in the lower portion of the eye.

To show further the long residence of the air mass above the inversion in the eye, forward and backward trajectories are computed by interpolating the hourly model output into 3-min intervals with air parcels released at various heights in the eye. Figure 6c presents the 32-h backward trajectory of a parcel ended at the inversion (i.e., 3.2 km) at the eye's center and originated at 10.5 km. One can see that the parcel descends cyclonically inward with variable rates. In 32 h, it is displaced downward at an average rate of 6.5 cm s⁻¹. Therefore, we may conclude that most of the air in the eye region must have remained in the eye for a very long time, perhaps since it was first enclosed in the eye.

c. Gravity–inertial oscillations in the eye

Pronounced fluctuations in vertical motion also occur in the eye (Fig. 7), with an oscillation period of about 3 h. This period is just resolvable from the hourly model output and is close to the oscillation of the updrafts in the eyewall. The amplitude of the fluctuation varies from − 0.5 to +0.5 m s⁻¹, with the more significant oscillations located above the warm core. By comparison,

initiated from the tropopause, is estimated at a rate of 5.3 cm s⁻¹, which is close to the mean descending rate (about 6–7 cm s⁻¹; see Fig. 5). In the minimum θ_e layer, the numerical diffusion is as significant as the vertical advection in increasing its local θ_e value; it tends to
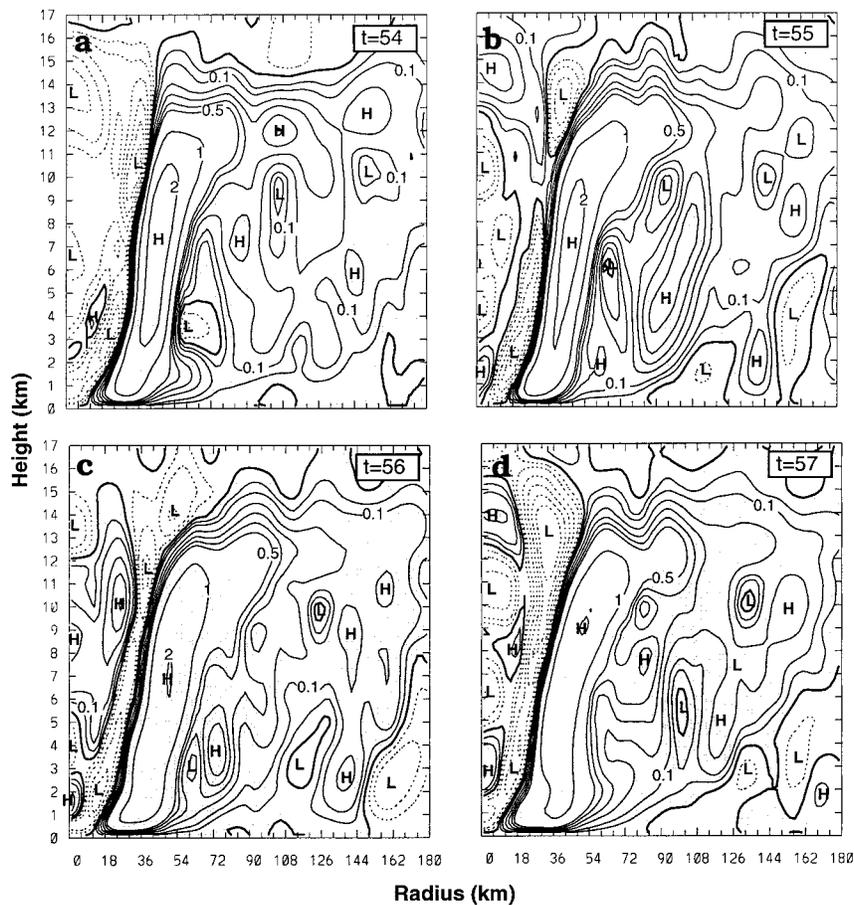
FIG. 8. Radial–height cross sections of azimuthally averaged vertical velocity with contours at 0, ($\pm$)0.05, ($\pm$)0.1, ($\pm$)0.2, ($\pm$)0.3, ($\pm$)0.4, ($\pm$)0.5, ($\pm$)1.0, and ($\pm$)2.0 m s^{-1} from (a) 54-, (b) 55-, (c) 56-, and (d) 57-h integration. Solid (dashed) lines are for upward (downward) motions.

upward motion persists in the lowest 1–2 km, in agreement with the foregoing discussions pertaining to Fig. 3h and Fig. 5. Of particular interest is that a deep layer of upward motion sometimes appears at the center of the eye. This finding is at odds with the traditional concept of subsiding motion in the eye region inferred from the buildup of a warm core in the eye. Such a fluctuation in W has also been noted by Franklin et al. (1988) in the eye of Hurricane Gloria (1985) during its intensifying stage.

Our results indicate that the W fluctuations in the eye are a typical feature during the development of a hurricane. However, any upward motion in the eye must be transitory and is associated with the propagation of inertial–gravity waves. Otherwise, the structure of the warm core cannot be maintained. To better examine the time evolution of W at the center of the eye, Fig. 8 presents the vertical cross sections of the axisymmetric W field at 1-h intervals from 54 to 57 h when the wave propagation is most pronounced. It is evident that there is little change in the basic pattern of the eyewall updraft, except at its top (i.e., near the tropopause) where

an (unbalanced) undulating appearance occurs in association with the return inflow. Since the static stability near the tropopause is large, any unbalanced flow, for example, generated by overshooting convection (cf. Figs. 8 and 3c), must appear in the form of inertial–gravity waves propagating in both the azimuthal and radial directions with a frequency lying between the Brunt–Väisälä and local inertia frequencies. Because the volume decreases toward the eye, the amplitude of the oscillation produced by inward propagating waves would be larger in the eye than in the outer regions. This interpretation is consistent with the development of the larger spatial and temporal variations of W in the eye (Figs. 8a–d). Despite the oscillations, the mean W is still dominated by weak subsidence at the center of the eye (see Fig. 5) and stronger descent at the inner edge of the eyewall (Figs. 8a–d).

Based on our modeling results and those from previous observations (e.g., Franklin et al. 1988), we conjecture that fluctuations associated with inertial–gravity waves are the basic characteristics of the eye and the eyewall. Of course, detailed high-resolution observa-
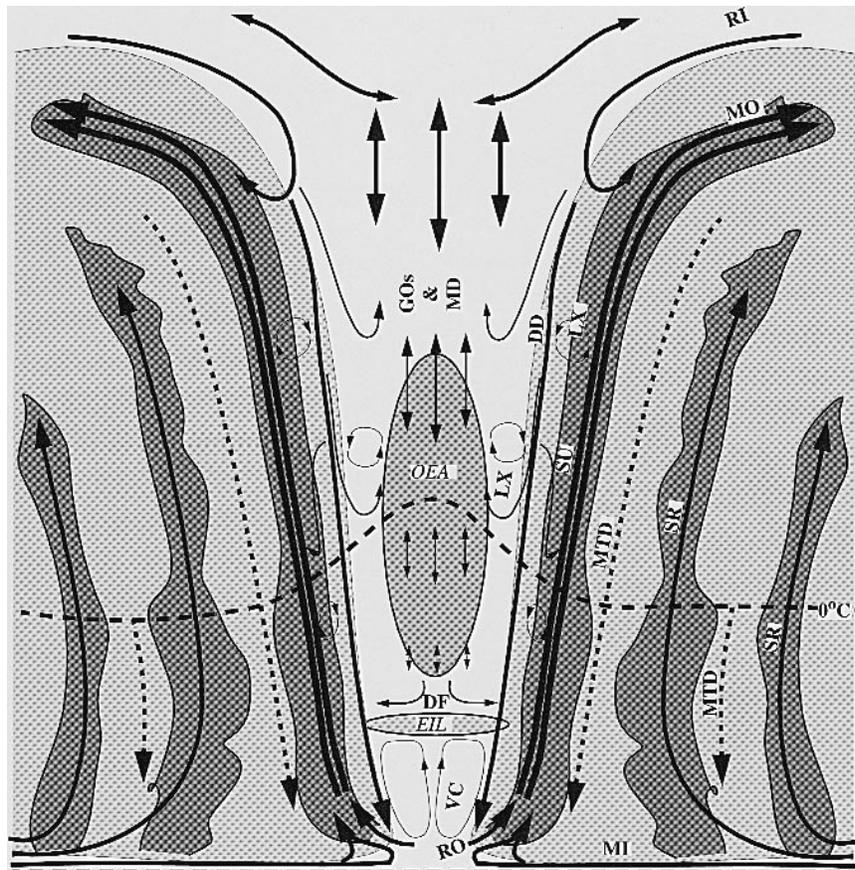
FIG. 9. A schematic (radial–height) conceptual model of a mature hurricane in the inner-core region. The light-shading areas indicate regions with cloud and precipitation. The dark regions represent the convective eyewall and spiral rainbands. The slash-hatched areas represents the eye inversion layer (EIL) and the cross-hatched regions is the occluded eye air (OEA) with low θ_e. The freezing level is marked with a dashed line. MTD and SR stand for moist downdrafts between the convective bands and spiral rainband updrafts, respectively. Refer to the text for the meaning of other symbols.

tions, particularly in the upper troposphere, are needed to verify this conjecture. If it is proved valid, then instantaneous or point observations would be inadequate in capturing certain important features of the eye and the eyewall.

d. Conceptual model

Based on our findings, we propose a conceptual model that describes the axisymmetric structures in the inner core of a mature hurricane (see Fig. 9). The main ingredients of the model consist of the basic and local circulations, the inertial–gravity wave oscillations, and the process of lateral mixing.

The basic circulations include a layer of main inflow (MI) below 1.5 km in the MBL, a sloping updraft (SU) in the eyewall, a main outflow (MO) in the upper troposphere, and a mean descent (MD) in the eye. The first three airstreams, often referred to as the secondary circulation, have been well expounded in previous studies

(e.g., Ooyama 1982; Willoughby 1988). Although the MI originates from the far outer regions, it intensifies mostly in the inner core as a result of the deepening of the storm and the transfer of angular momentum. Its speed reaches a maximum slightly outside the RMW and then decelerates rapidly toward the center of the eye. The MI plays an important role in feeding the high-θ_e air to the eyewall convection. The SU has its roots in the MBL and it is fed by the high-θ_e air from the MI and the eye. In the midtroposphere, the SU is characterized by a weak, divergent, radial outflow except at the melting level. More pronounced divergent outflow (i.e., MO) appears near the top of the eyewall. The development of the intense low-level MI/upper-level MO suggests that the eyewall updraft is dynamically organized although it is driven by latent heat release (Houze 1993). Although the MD generally characterizes the eye in a time-averaged sense, it is interrupted by pronounced spatial and temporal fluctuations associated with inertial–gravity waves. The MD advects the warm

core and the minimum θ_e layers downward, thereby strengthening the inversion below. The MD at the center of the eye, averaged over a 40-h period, reaches values of 5 cm s^{-1} or 3.6 km per day. Such slow descent under the inertially stable conditions suggests that the air in the eye, particularly the minimum θ_e air, may have remained there since it was first enclosed. This interpretation is also supported by our trajectory calculations.

The local vertical circulations include a radially narrow zone of dry downdraft (DD) along the inner edge of the eyewall, a return inflow (RI) near the tropopause, a return outflow (RO) from the bottom layer of the eye, a divergence flow (DF) in the inversion, and a frictionally forced vertical circulation (VC) below the inversion. Note that the inversion weakens toward the eyewall. The altitude of the inversion remains nearly constant but its intensity increases with time as a result of subsidence aloft and ascent below. These local circulations are mainly forced by the basic circulations, but they also contribute significantly to the development of the hurricane. The RI, a branch of the local upper-eye vertical circulation, is generated by the release of latent heat and momentum sources in the upper eyewall. It streams inward from above the eyewall, descends after entering the eye, and finally intrudes into the eyewall. The RI is the basic mass source that initiates and feeds the strong subsidence in the eye, particularly the penetrative DD. It induces convergence toward the eye and appears to be responsible for the generation of inertial–gravity waves. While the DD is initiated by the RI, its further downward development to the MBL is believed to be due to the sublimative/evaporative cooling of detrained condensates from the eyewall (Gray and Shea 1973) and the compensating subsidence associated with the local heating in the eyewall (Shapiro and Willoughby 1982). The VC is frictionally forced (Holton 1992) and influenced by penetrative DDs; it induces maximum ascent at the center of the eye and recycles the mass into the eyewall through the low-level RO. Note that Willoughby (1998) defined this descending motion as the saturated downdrafts. We prefer to call it dry downdraft because it is located in the zone of maximum relative humidity gradients (between 50% and 90%) where the sublimation and evaporation rates are pronounced.

The other two kinematic elements, inertial–gravity oscillations (GOs) and lateral mixing (LX), also play a role in determining the time evolution of the inner-core structures. The GOs are generated in the upper eye by the RI; they weaken (intensify) outward (inward) from the eyewall and also diminish downward. The GOs appear to account primarily for the generation of the fluctuating W in the eye. We speculate that the GOs may affect the size of the eye at certain levels by changing the slope of the eyewall. Although few direct observations are available to show the presence of GOs, the fluctuating W in the eye of Hurricane Gloria (1985) analyzed by Franklin et al. (1988) supports indirectly our model-simulated results. The symbol LX denotes both entrainment and detrainment of individual flow elements described above as well as any diffusive effects. As will be shown in a forthcoming article, the upper-level RI and part of the DD can be considered as detrained masses from the eyewall that help drive or modify the local circulations. Numerical diffusive effects in the model are parameterized by subgrid-scale eddy mixing processes. They depend on the gradients of the quantities being diffused, the deformation of the flow, and the Richardson number. As such, diffusive effects are generally less significant in the eye, except in the minimum θ_e layer. However, they are not negligible in the SU and DD.

5. Asymmetric structures and the trochoidal oscillation

After discussing the axisymmetric structures of the storm, it is natural to examine the degree of asymmetry. Figure 10 displays the azimuthal–height cross sections of the simulated 3D storm-relative flows and radar reflectivity at different radii. Three radii are displayed: (a) the inner edge (30 km), (b) the central portion (42 km), and (c) the outer edge of the eyewall (90 km). One can see clearly that the fields are not axisymmetric but show strong variations with azimuth, as have also been shown in Part I. For example, the tangential winds vary from 60 to 80 m s^{-1} below 5 km, and exhibit a maximum in a zone sloping upwind with height in the southwest quadrant in the eyewall (Figs. 10b,c). (Note that the total surface winds are peaked in the northwestern quadrant.) The azimuthal variation is smaller in the outer than the inner radii (cf. Figs. 10a–c). Likewise, radial winds above 2 km change from a 10 m s^{-1} outflow in one quadrant to a 10 m s^{-1} inflow in another. On average, the net radial flow in the midtroposphere is small (cf. Figs. 10b and 3f). Furthermore, there is a deep layer of radial inflow across the eyewall at wavenumber 2 below 9 km and at wavenumber 1 above. Note the systematic MO in the 10–14-km layer that is consistent with the axisymmetric structures (cf. Figs. 3f and 10a). By comparison, the RI is less organized. It occurs mainly atop intense updrafts (Figs. 10a,d) as part of the convectively driven divergent outflow. It descends as it moves into the eye and plays an important role in the initiation of the dry DDs (Figs. 10b,e).

Similarly, the reflectivity and W fields indicate that the eyewall is composed of a series of inhomogeneous updraft cells (>6 m s^{-1}) with moist downdrafts in between. The moist downdrafts are more pronounced below the melting level, for example, in the northwest and southeast quadrants (Fig. 10e). In contrast, the distribution of DDs corresponds closely to the distribution of the radial inflow. The DDs are initiated in the upper troposphere, and they penetrate *in a slantwise fashion* to the bottom of the eye (Figs. 10d–f). For instance, the DD that penetrates down to 3 km in the south quadrant appears to be initiated at 12–14 km in the west to north
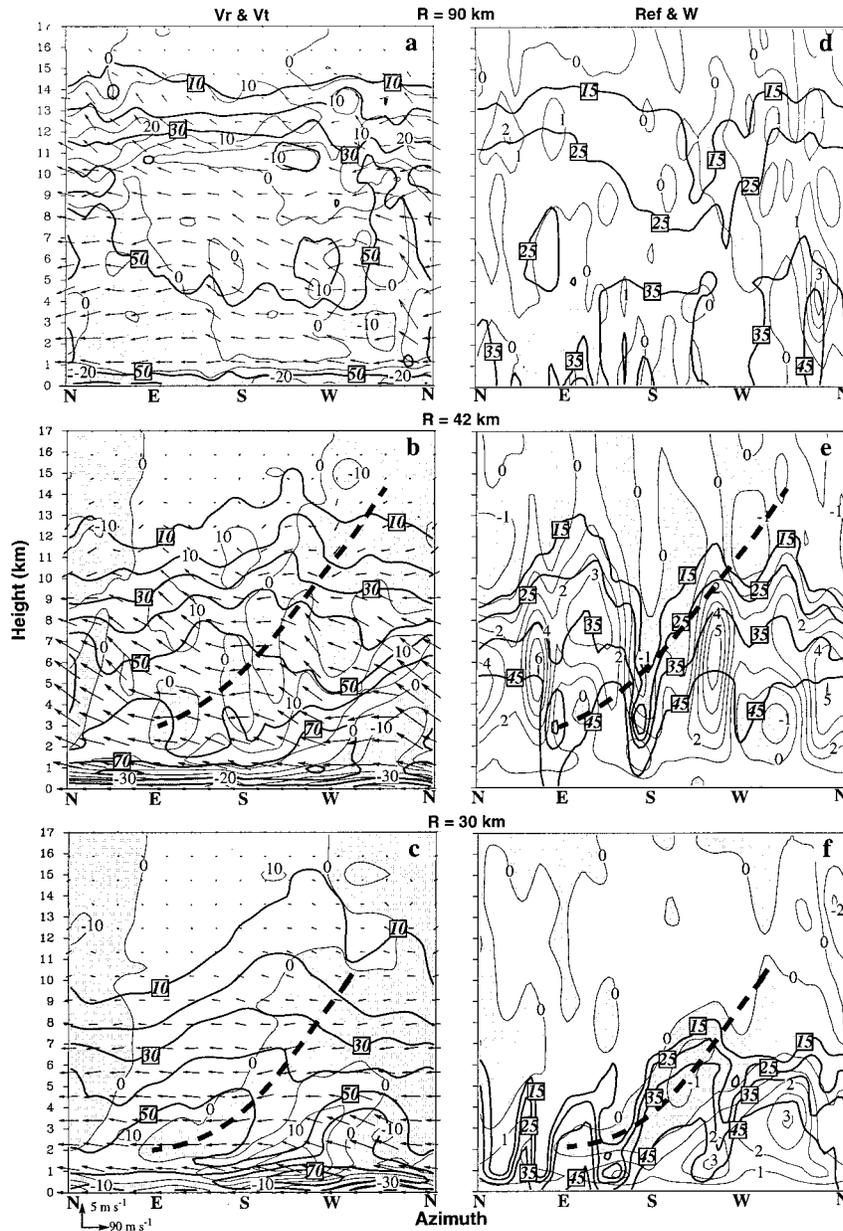
FIG. 10. Azimuth–height cross sections of (a)–(c) storm-relative tangential (thick lines) and radial (thin lines) winds (inflow regions are shaded) at intervals of 10 m s^{-1}, superposed with cross-sectional flow vectors; (d)–(f) radar reflectivity (thick lines, every 10 dbZ) and vertical velocity (thin lines, every 1 m s^{-1}, downdrafts are shaded) taken along a circle with radii of 90 (top panels), 42 (middle panels), and 30 km (bottom panels), respectively, from the 56-h integration. Thick dashed lines denote the axis of a major radial inflow and its associated descending motion.

quadrant (cf. Figs. 10b and 10e). The same can be said for the major DD at radius of 30 km (cf. Figs. 10c and 10f). The downward troughing of the reflectivity contour associated with the DDs suggests the importance of sublimative/evaporative cooling in driving the penetrative DDs. Note that the DDs are not located in the same azimuthal direction as the updrafts. Because the tangential velocity varies with radial distance, the DDs

are displaced downstream and slightly inward of the updrafts. Again, Kurihara and Bender (1982) show little evidence of azimuthally slantwise downdraft structures due to their use of a convective adjustment scheme.

In response to the advective effect of the strong tangential flow that varies with height, the contour lines of all plotted variables, including the up- (down-) drafts in the eyewall and the tangential and radial flows, tend
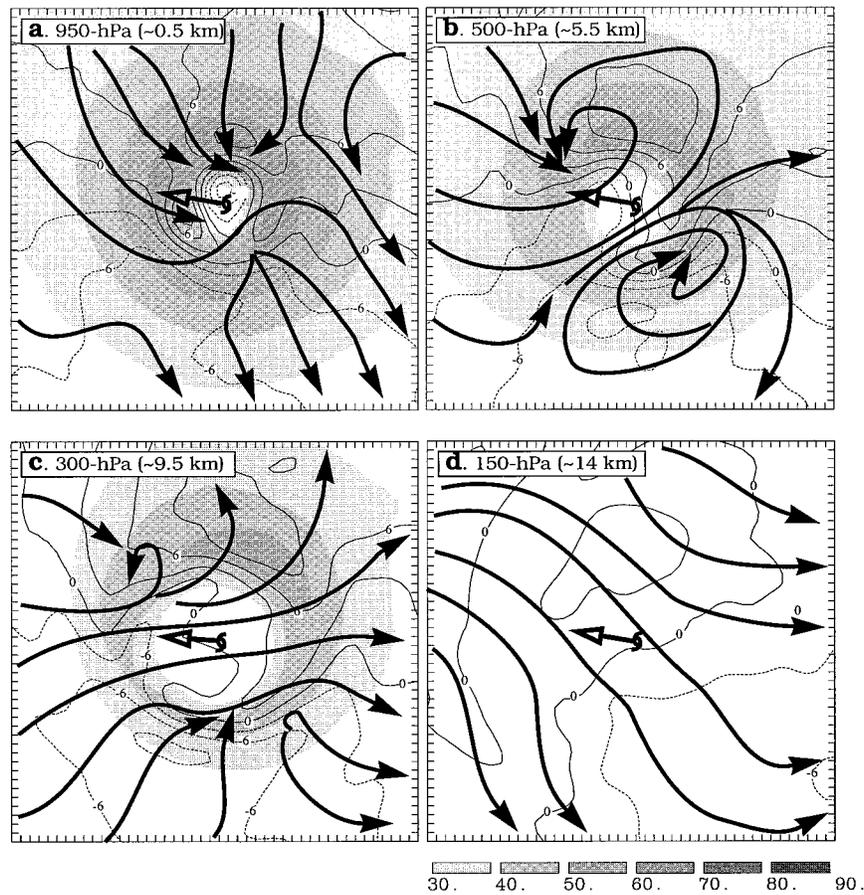
FIG. 11. Streamlines (thick solid with arrows) of asymmetric wind perturbations at (a) 950, (b) 500, (c) 300, and (d) 150 hPa, superposed with the perturbation speeds (thin lines, solid/positive and dashed/negative) at interval of 3 m s^{-1} and the total winds (shaded, every 10 m s^{-1} starting from 30 m s^{-1}), that are temporally averaged between the 48- and 60-h integrations. The center and propagation direction of the storm is denoted by a hurricane symbol and hollow arrow. The intervals marked on the frame is 6 km.

to tilt in the downshear direction (Fig. 10), in agreement with the observations by Marks et al. (1992), Lee et al. (1994), and Roux and Marks (1996). Note that the axis of the radial outflow (inflow) lies above (below) the axis of the tangential flow. This configuration can be explained by the principle of conservation of angular momentum. As an example, consider a parcel of air at a certain level initially at equilibrium with the environmental tangential flow. As the parcel moves upward from its initial position, it will have an excess of angular momentum over its new environment because the axis of tangential wind tilts downshear with height. To conserve angular momentum, a rising parcel must move outward so that the axis of radial outflow lies above the axis of the tangential wind. The opposite is true when air parcels move downward. They would move inward with the result that the axis of radial inflow lies below the axis of tangential wind. Depending on the local tangential shear above the MI layer, the vertical tilts of updrafts and downdrafts vary from nearly upright to a

slope of 1:1.5. Because the tangential and radial flows are distributed asymmetrically, except above 8 km, the updrafts and downdrafts as well as other properties in the eyewall change rapidly with time relative to one another, a feature also noted by Marks et al. (1992). Typically, the timescale of change can be estimated by noting that it takes 1–1.5 h for an updraft cell to be advected in a complete circle in the eyewall.

Figure 11 shows the streamlines computed from the 12-h-averaged (48–60 h of integration) asymmetric perturbation wind components $(V'_t)_a$ and $(V'_r)_a$ [see Eq. (6)], their speed, and the total wind **V** [see Eq. (5)] at four different levels. The main purpose of producing this figure is to compare it with recent Doppler radar analyses of the asymmetric structures of hurricanes by Marks et al. (1992) and Roux and Viltard (1995), who noted the presence of wavenumber 1 and 2 disturbances. However, unlike in their approach, the asymmetric perturbation flows in the present case are obtained by removing the deep-layer mean wind instead of the height-

dependent mean wind. Thus, as mentioned in section 3a, the asymmetric perturbation flows so obtained are almost equivalent to the storm-relative flows.

Two features are worthy of discussion. The first is the asymmetric isotach pattern characterized by a positive perturbation in the north and a negative perturbation in the south (Figs. 11a–d). This pattern extends vertically throughout the troposphere in agreement with aircraft observations in Andrew (Willoughby and Black 1996). The distribution of the perturbation wind confirms the idea of the so-called ''hazardous semicircle'' with more violent winds at the northern semicircle. The second feature depicted by the streamlines is the asymmetrical wavenumber-1 source–sink couplet at the lower levels and the dual-gyre couplet at the higher levels. The source–sink couplet is located in the eyewall (Fig. 11a). Mass converges toward the sink situated in the north-northeast quadrant and diverges away from the source in the southeast quadrant. The picture is consistent with the structure of the low-level storm-relative flow shown in Fig. 1b as a result of the faster movement of the storm relative to its environment. The distribution of the convergence and divergence implies that the northwest quadrant is most favored for the sustained development of deep convection.

The dual-gyre structure first appears at 850 hPa (not shown) and it extends to the upper outflow layer (Figs. 11b–d). Like the source–sink couplet, the gyre couplet is also located in the eyewall, with the cyclonic (anticyclonic) gyre in the northwest (southeast) quadrant, as also noted by Mark et al. (1992) in Norbert. An idealized numerical study by Peng and Williams (1990) shows that the inner-core gyres can result from the nonlinear interaction between the mean flow and the storm's movement. It should be mentioned that the acrosseye flows above the MBL are associated with the perturbation gyre couplet rather than the environmental ''ventilating'' flow through the eye.

The overall asymmetric flow structures, dominated by wavenumber 1, are similar to the Doppler analyses of hurricanes by Marks et al. (1992) and Roux and Viltard (1995), except for slight differences in the location of the gyres because the propagations of the storms relative to their environmental flows are not the same. These asymmetric perturbations are determined by nonlinear interaction between the mean tangential flow and the storm movement as discussed above.

It is known that the eye and circulation centers tend to be located closer to more intense convective areas (Willoughby et al. 1984b). Because the distribution of deep convection is asymmetric, the locations of the center tilt with height. As an example we show in Fig. 12 the time evolution of the departure of pressure center, defined as the horizontal distance of the upper-level center relative to the surface center. It is evident that the departure increases with height. The departure is large in the first few hours because the model is adjusting from an 18- to a 6-km grid size; it decreases rapidly
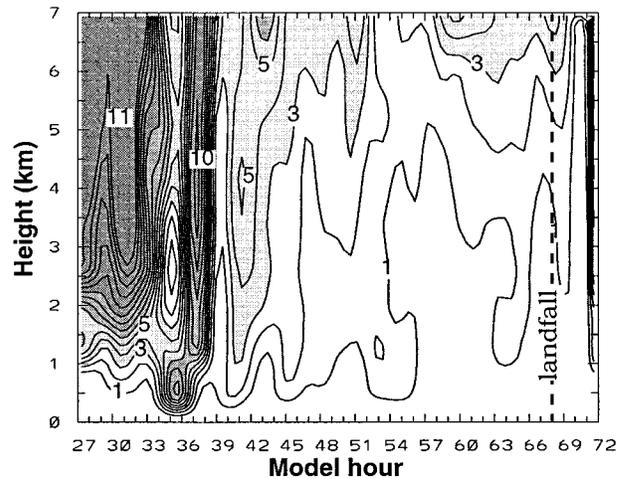

FIG. 12. The time–height cross section of the horizontal departure (km) of low pressure centers from the surface center.

afterward. Further decrease after this time is small. The evolution of the departure is well correlated with the intensification and symmetrization of the system (Carr and Williams 1989). The 5-km value in our simulation is close to the 3–4-km departure from the flow center found by Marks et al. (1992) and Roux and Marks (1996). In general, the slope of the axis of central pressure also fluctuates with time but it is nearly vertical below 5 km during the mature stage.

The asymmetric distribution of convective cells and their advection by the intense tangential flows tend to produce an elliptical eyewall and contribute to the trochoidal oscillation as the storm moves (Newman and Boyd 1962). The trochoidal oscillation in the tracks of hurricanes has been reported by Willoughby et al. (1984b), Roux and Viltard (1995), and Griffin et al. (1992). Figure 13a depicts the positions of the pressure center and the mean track derived from the hourly model output. A low-pass filter has been used to obtain the mean track. The trochoidal oscillation can be measured by the departure of the instantaneous position of the pressure center from the central position along the mean track at the same time. Figure 13b shows that the departure can be in both the lateral and longitudinal directions. The lateral and longitudinal departures can be as large as 20 km. Because the trochoidal oscillation is believed to be a direct response of the pressure center to the asymmetric distribution of convection in the eyewall, the more dominant the symmetric components are, the less is the track oscillation. Thus, the lateral and longitudinal departures decrease from 20 km in the first 15 h to 3–5 km in the second, and to <3 km in the final 15 h (Fig. 13b). Besides the departure in the track, trochoidal oscillation also causes large variations in the speed of propagation of the pressure center (Fig. 13c). The amplitude of variation about the mean is about 50% of the mean propagation speed of the storm ($\sim$8 m s^{-1}) during the intensifying stage. As the storm becomes
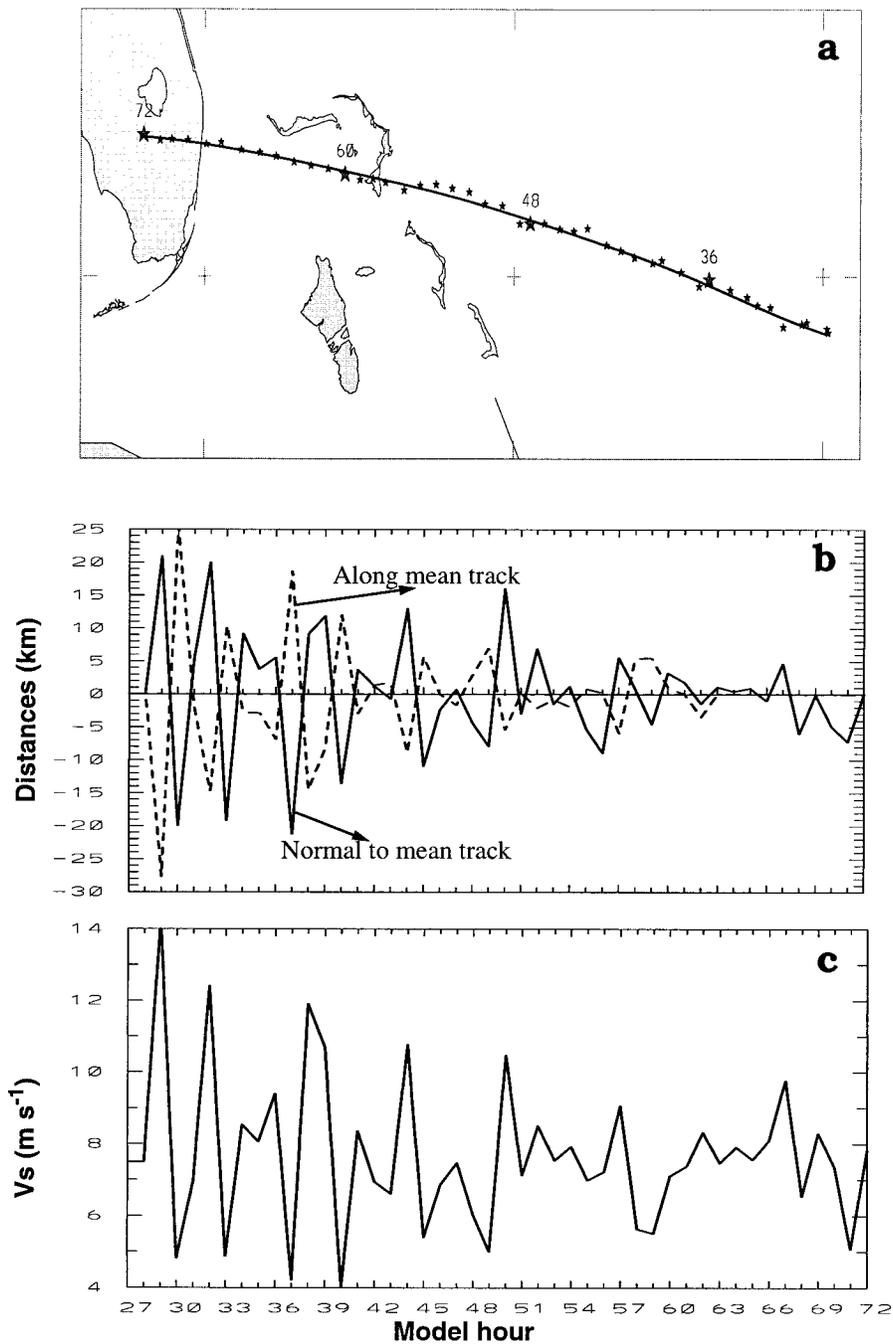
FIG. 13. (a) The track of the surface low pressure center, (b) the evolution of the departure (km) from the mean track in the longitudinal and lateral directions, and (c) the evolution of the instantaneous speed of the surface pressure center determined from the hourly model output.

more symmetrical at later stages, the amplitude of variation decreases and the pressure center propagates at a more uniform speed. The oscillation indicates a period of 3–4 h, which is the same as the temporal oscillations of the properties in the eye and the core of the hurricane (cf. Figs. 4 and 7). We should caution, however, that because the analysis is performed with hourly model output, only a 2–3-h period could be resolved.

6. Summary and conclusions

In this paper, a 72-h, high-resolution ($\Delta x = 6$ km), explicit simulation of Hurricane Andrew (1992) presented in Part I is analyzed to examine the kinematic and thermodynamic structures in the inner-core regions of the storm. The horizontal mean, the axisymmetric and asymmetric components of various variables, and

their time variations are obtained to yield the essential and persistent inner-core structures of the hurricane. Special attention is given to the organization and circulations in the eye and the eyewall as well as the interaction between these circulations. A conceptual axisymmetric model of the inner-core structures is presented. The most important results are summarized as follows.

- Dry downdrafts, about one order of magnitude stronger than the typical subsidence at the center of the eye, occur in a 6–12-km zone at the inner edge of the eyewall (with a relative humidity between 60% and 90%). Their extent in the azimuthal direction is often greater than 100 km. The downdrafts originate from the return inflow situated above the level of outflow in the eyewall. They appear to be driven by the compensating subsistence and sublimative/evaporative cooling of detrained hydrometeors from the eyewall. The distribution of the dry downdrafts corresponds closely to that of the radial inflow of midlevel dry/cold air. The downdrafts penetrate azimuthally downshear to the surface, along the slantwise inner edge of the eyewall, and can be treated as an interface between the eye and the eyewall. Part of the downdraft air may reenter the eyewall near the bottom of the eye after it has been heated by the surface sensible fluxes.
- The air in the eye can be divided into two parts, separated by an inversion at an altitude of 2–3 km. A warm/dry air mass lies above the inversion and a warm/moist pool lies below. The air mass aloft is radially secluded, except through horizontal diffusion, due to the presence of strong inertial stability. On average, it descends at a rate of 5–6 cm s^{-1} to warm and dry the eye and deepens the storm. However, the instantaneous descent can reach values of 1 m s^{-1} and it is characterized by significant inertial–gravity oscillations. The descending air appears to diverge at the level of the inversion. As a result, the air mass above the inversion, including the minimum θ_e layer, may be secluded at the time when the eyewall is formed, and then it remains in the eye for several days.
- In contrast, the warm/moist pool at the bottom of the eye represents a mixture of air from the main inflow and the downdraft along the inner edge of the eyewall that is in equilibrium with the low-level return outflow. The air mass is warm and moist because of the upward fluxes from the underlying warm ocean. At the center of the eye, localized ascent dominates as part of a secondary circulation caused by frictional convergence and penetrative DDs. This localized secondary circulation helps pump heat and moisture upward so that θ_e is maximized near the center of the eye. The return outflow then transports the high-θ_e air into the eyewall to intensify the development of convection.
- Our model simulation shows pronounced fluctuations in air motion in both the eye and the eyewall. The

instantaneous vertical motion in the eye varies within ± 0.5 m s^{-1}, with more significant oscillations above the warm core. It is found that a deep layer of upward motion can sometimes appear at the center of the eye, contrary to the traditional concept of subsidence in the eye. We are of the opinion that these fluctuations are part of the convectively forced inertial–gravity waves. We also found that the intensity of updrafts in the eyewall fluctuates as the eyewall contracts and the storm deepens. Nevertheless, the fluctuations are transient in nature since the mean vertical motion in the eye is still dominated by weak subsidence at the center and stronger descent at the inner edge of the eyewall. Based on the results presented herein and in previous observations, we argue that this type of wave propagation is a basic characteristic of the eye and the eyewall.

- It is shown that all the fields in the inner-core regions are highly asymmetric and associated with the asymmetric distribution of deep convection in the eyewall and the propagation of inertial–gravity waves. In addition, all the fields tilt more or less with height radially outward and azimuthally downshear. The asymmetric structures, the vertical tilt, and inertial–gravitational fluctuations all contribute to the trochoidal oscillation of the storm track and the movement of the storm. The storm-scale flows are also asymmetric. A mass source–sink couplet occurs in the boundary layer and dual cyclonic–anticyclonic gyres occur above with the cyclonic gyre and the anticyclonic gyre distributed, respectively, in the northwest and southeast quadrants. However, the degrees of asymmetry decrease with time as the eyewall contracts and the storm deepens.
- A varying vertical shear and veering of the horizontal mean wind in the inner core exist during the rapid deepening stage of Andrew. However, the deep-layer area-averaged wind appears to represent well the motion of the storm. On average, the differences between the deep-layer mean flows and the movement of the storm are less than 1.0 m s^{-1}. It is found that the horizontal mean flow at an altitude of 4.5 km within a radius of 150 km represents extremely well the motion of the storm, suggestive of a stronger steering at the middle layer. Thus, more accurate short-time track forecasts can be achieved by examining the area-averaged or deep-layer mean winds below 12 km.

It should be mentioned that the above conclusions are obtained from an explicit simulation of a single hurricane in which some deficiencies still exist due partly to the lack of observations in generating the model initial conditions and partly to the use of the 6-km grid length that is still too coarse to resolve deep convection in the eyewall. Nevertheless, the many agreements between the simulated hurricane and the observed Andrew presented in Part I led us to the belief that the basic conclusions presented here are relevant to real tropical

storms. In a forthcoming article, we will attempt to provide a quantitative understanding of the inner-core dynamics of the storm by calculating the budgets of the mass, momentum, and heat.

REFERENCES

Anthes, R. A., 1982: *Tropical Cyclones—Their Evolution, Structure, and Effects. Meteor. Monogr.,* No. 41, Amer. Meteor. Soc., 208 pp.

Bender, M. A., 1997: The effect of relative flow on asymmetric structure in the interior of hurricanes. *J. Atmos. Sci.,* **54,** 703–724.

Carr, L. E., III, and R. T. Williams, 1989: Barotrophic vortex stability to perturbations from axisymmetry. *J. Atmos. Sci.,* **46,** 3177–3196.

Dong, K., and C. J. Neumann, 1986: The relationship between tropical cyclone motion and environmental geostrophic flows. *Mon. Wea. Rev.,* **114,** 115–122.

Eastman, J. L., 1995: Numerical simulation of Hurricane Andrew— Rapid intensification. Preprints, *21st Conf. on Hurricanes and Tropical Meteorology,* Miami, FL, Amer. Meteor. Soc., 111–113.

Elsberry, R. L., 1995: Tropical cyclone motion. Global Perspectives on Tropical Cyclones, WMO/TD-693, 106–191.

Emanuel, K. A., 1986: An air–sea interaction theory for tropical cyclones. Part I: Steady-state maintenance. *J. Atmos. Sci.,* **43,** 585–604.

——, 1997: Some aspects of hurricane inner-core dynamics and energetics. *J. Atmos. Sci.,* **54,** 1014–1026.

Franklin, J. L., 1990: Dropwindsonde observations of environmental flow of Hurricane Josephine (1984): Relationship to vortex motion. *Mon. Wea. Rev.,* **118,** 2732–2744.

——, S. J. Lord, and F. D. Marks Jr., 1988: Dropwindsonde and radar observations of the eye of Hurricane Gloria. *Mon. Wea. Rev.,* **116,** 1237–1244.

——, ——, S. E. Feuer, and F. D. Marks Jr., 1993: The kinematic structure of Hurricane Gloria (1985) determined from nested analyses of dropwindsonde and Doppler radar data. *Mon. Wea. Rev.,* **121,** 2433–2450.

Gamache, J. F., R. A. Houze Jr., and F. D. Marks Jr., 1993: Dual-aircraft investigation of the inner core of the Hurricane Norbert. Part III: Water budget. *J. Atmos. Sci.,* **50,** 3220–3243.

George, J. E., and W. M. Gray, 1976: Tropical cyclone motion and surrounding parameter relationships. *J. Appl. Meteor.,* **15,** 1252–1264.

Gray, W. M., 1991: Comments on "Gradient balance in tropical cyclones." *J. Atmos. Sci.,* **48,** 1201–1208.

——, and D. J. Shea, 1973: The hurricane's inner core region. II. Thermal stability and dynamic characteristics. *J. Atmos. Sci.,* **30,** 1565–1576.

Griffin, J. S., R. W. Burpee, S. D. Marks Jr., and J. L. Franklin, 1992: Real-time airborne analysis of aircraft data supporting operational hurricane forecasting. *Wea. Forecasting,* **7,** 480–490.

Guinn, T. A., and W. H Schubert, 1993: Hurricane spiral bands. *J. Atmos. Sci.,* **50,** 3380–3403.

Hawkins, H. F., and S. M. Imbembo, 1976: The structure of a small, intense hurricane, Inez 1966. *Mon. Wea. Rev.,* **104,** 418–442.

Holland, G. J., 1984: Tropical cyclone motion: A comparison of theory and observation. *J. Atmos. Sci.,* **41,** 68–75.

——, 1997: The maximum potential intensity of tropical cyclones. *J. Atmos. Sci.,* **54,** 2519–2541.

——, and R. T. Merrill, 1984: On the dynamics of tropical cyclone structural changes. *Quart. J. Roy. Meteor. Soc.,* **110,** 723–745.

Holton, J. R., 1992: *An Introduction to Dynamic Meteorology.* Academic Press, 511 pp.

Houze, R. A., Jr., 1993: *Cloud Dynamics.* Academic Press, 573 pp.

——, F. D. Marks Jr., and R. A. Black, 1992: Dual-aircraft investigation of the inner core of the Hurricane Norbert. Part II: Mesoscale distribution of ice particles. *J. Atmos. Sci.,* **49,** 943–962.

Jordan, C. L., 1952: On the low-level structure of the typhoon eye. *J. Meteor.,* **9,** 285–290.

Jorgensen, D. P., 1984a: Mesoscale and convective scale characteristics of nature hurricanes. Part I: General observations by aircraft. *J. Atmos. Sci.,* **41,** 1268–1285.

——, 1984b: Mesoscale and convective scale characteristics of nature hurricanes. Part II: Inner core structure of Hurricane Allen (1980). *J. Atmos. Sci.,* **41,** 1287–1311.

Kurihara, Y., and M. A. Bender, 1982: Structure and analysis of the eye of a numerically simulated tropical cyclone. *J. Meteor. Soc. Japan,* **60,** 381–395.

Lee, W.-C., F. D. Marks, and R. E. Carbone, 1994: Velocity track display—A technique to extract real-time tropical cyclone circulations using a single airborne Doppler radar. *J. Atmos. Oceanic Technol.,* **11,** 337–356.

Liu, Y., D.-L. Zhang, and M. K. Yau, 1997: A multiscale numerical study of Hurricane Andrew (1992). Part I: An explicit simulation. *Mon. Wea. Rev.,* **125,** 3073–3093.

Marks, F. D., Jr., 1985: Evolution and structure of precipitation in Hurricane Allen (1980). *Mon. Wea. Rev.,* **113,** 909–930.

——, and R. A. Houze Jr., 1987: Inner-core structure of Hurricane Alicia from airborne Doppler-radar observations. *J. Atmos. Sci.,* **44,** 1296–1317.

——, ——, and J. F. Gamache, 1992: Dual-aircraft investigation of the inner core of the Hurricane Norbert. Part I: Kinematic structure. *J. Atmos. Sci.,* **49,** 919–942.

Newman, S., and J. G. Boyd, 1962: Hurricane movement and variable location of high intensity spot in wall cloud radar echo. *Mon. Wea. Rev.,* **90,** 371–374.

Nicholls, M. E., and R. A. Pielke, 1995: A numerical investigation of the effect of vertical shear on tropical cyclone intensification. Preprints, *21st Conf. on Hurricanes and Tropical Meteorology,* Miami, FL, Amer. Meteor. Soc., 339–341.

Ooyama, K., 1982: Conceptual evolution of the theory and modeling of the tropical cyclone. *J. Meteor. Soc. Japan,* **60,** 369–380.

Peng, M. S., and R. T. Williams, 1990: Dynamics of vortex asymmetries and their influence on vortex motion on a β-plane. *J. Atmos. Sci.,* **47,** 1987–2003.

Powell, M. D., 1982: The transition of the Hurricane Frederic boundary-layer wind field from the open Gulf of Mexico to landfall. *Mon. Wea. Rev.,* **110,** 1912–1932.

——, and S. H. Houston, 1996: Hurricane Andrew's landfall in Florida. Part II: Surface wind fields and potential real-time application. *Wea. Forecasting,* **11,** 329–349.

Riehl, H., 1948: A radiosonde observation in the eye of a hurricane. *Quart. J. Roy. Meteor. Soc.,* **74,** 194–196.

——, 1954: *Tropical Meteorology.* McGraw-Hill, 392 pp.

Rotunno, R., and K. A. Emanuel, 1987: An air–sea interaction theory for tropical cyclones. Part II: Evolutionary study using a nonhydrostatic axisymmetric numerical model. *J. Atmos. Sci.,* **44,** 542–561.

Roux, F., and N. Viltard, 1995: Structure and evolution of Hurricane Claudettte on 7 September 1991 from airborne Doppler radar observation. Part I: Kinematics. *Mon. Wea. Rev.,* **123,** 2611–2639.

——, and F. D. Marks, 1996: Extended Velocity Track Display (EVTD): An improved processing method for Doppler radar ob-

servations of tropical cyclones. *J. Atmos. Oceanic Technol.,* **13,** 875–899.

Schubert, W. V., and J. J. Hack, 1982: Inertial stability and tropical cyclone development. *J. Atmos. Sci.,* **39,** 1687–1697.

Shapiro, L. J., and H. E. Willoughby, 1982: The response of the balanced hurricanes to local sources of heat and momentum. *J. Atmos. Sci.,* **39,** 378–394.

——, and M. T. Montgomery, 1993: A three-dimensional balance theory for rapidly rotating vortices. *J. Atmos. Sci.,* **50,** 3322–3335.

Shea, D. J., and W. M. Gray, 1973: The hurricane's inner core region. I. Symmetric and asymmetric structure. *J. Atmos. Sci.,* **30,** 1544–1564.

Simpson, R. H., 1952: Exploring the eye of Typhoon ''Marge,'' 1951. *Bull. Amer. Meteor. Soc.,* **33,** 286–298.

Smith, R. K., 1980: Tropical cyclone eye dynamics. *J. Atmos. Sci.,* **37,** 1227–1232.

Stear, J. R., 1965: Sounding in the eye of Hurricane Arlene to 108760 feet. *Mon. Wea. Rev.,* **93,** 380–382.

Tripoli, G. J., 1992: An explicit three-dimensional nonhydrostatic numerical simulation of a tropical cyclone. *Meteor. Atmos. Phys.,* **49,** 229–254.

Willoughby, H. E., 1979: Forced secondary circulations in hurricanes. *J. Geophys. Res.,* **84,** 3173–3183.

——, 1988: The dynamics of the tropical cyclone core. *Aust. Meteor. Mag.,* **36,** 183–191.

——, 1990: Temporal changes of the primary circulation in tropical cyclones. *J. Atmos. Sci.,* **47,** 242–264.

——, 1992: Linear motion of a shallow-water barotropic vortex as an initial-value problem. *J. Amos. Sci.,* **49,** 2015–2031.

——, 1995: Mature structure and evolution. Global Perspectives on Tropical Cyclones, WMO/TD-693, 21–62.

——, 1998: Tropical cyclone eye thermodynamics. *Mon. Wea. Rev.,* **126,** 3053–3067.

——, and P. G. Black, 1996: Hurricane Andrew in Florida: Dynamics of a disaster. *Bull. Amer. Meteor. Soc.,* **77,** 543–549.

——, J. A. Clos, and M. G. Shoreibah, 1982: Concentric eyewalls, secondary wind maxima, and the evolution of the hurricane vortex. *J. Atmos. Sci.,* **39,** 395–411.

——, H. L. Jin, S. J. Lord, and J. M. Piotrowicz, 1984a: Hurricane structure and evolution as simulated by an axisymmetric, non-hydrostatic numerical model. *J. Atmos. Sci.,* **41,** 1169–1186.

——, F. D. Marks Jr., and R. J. Feinberg, 1984b: Stationary and moving convective bands in hurricanes. *J. Atmos. Sci.,* **41,** 3189–3211.

Zhang, D.-L., Y. Liu, and M. K. Yau, 1999: Surface winds at landfall of Hurricane Andrew (1992)—A reply. *Mon. Wea. Rev.,* **127,** 1711–1721.